

Binding energy of polaronic trions and biexcitons in CsPbBr₃ nanocrystals

José L. Movilla

Dept. d'Educació i Didàctiques Específiques, Universitat Jaume I, 12080, Castelló, Spain

Josep Planelles, Juan I. Climente

*Dept. de Química Física i Analítica, Universitat Jaume I, 12080, Castelló, Spain**

(Dated: November 15, 2024)

The effect of polaron formation on the ground state of excitons, trions and biexcitons confined in CsPbBr₃ nanocrystals is studied in the framework of effective mass Hamiltonians, using a Haken-like (Bajaj) potential for carrier-phonon coupling. The binding energy of trions agrees well with that observed in experiments, with position-dependent dielectric screening playing a significant role. For biexcitons, however, neither polaronic effects, nor dielectric confinement, nor electronic correlations –here accounted for with a variational Quantum Monte Carlo method– suffice to explain the large binding energies reported by single nanocrystal spectroscopy experiments. This result reinforces the hypothesis that biexcitons polarize the perovskite lattice differently from excitons and trions.

PACS numbers:

I. INTRODUCTION

CsPbX₃ (X=Cl,Br,I) nanocrystals (NCs) combine the outstanding optoelectronic properties of lead halide perovskites with the tunability of quantum and dielectric confinement.^{1–4} Understanding the interactions among particles confined inside such systems is a prerequisite for eventual applications. In the last years, a large number of experimental studies have gone beyond exciton (X) complexes to address trions (X*) and biexcitons (BX).^{5–22} The interest of X* is largely related to the fact that they combine the optical response of X with the high sensitivity to external electric fields of charged species, which is convenient for field-modulated devices.²³ BX in turn are involved in several potential applications, including lasers, LEDs and quantum light sources.^{8,20} Prospects of BX exploitation in CsPbX₃ NCs are backed up by near-unity quantum yields, which result from the fast radiative rates outcompeting Auger processes.²⁴

The binding energy of X* and BX is a key figure quantifying the spectral shift of these species with respect to X, as well as the strength of the charge-X (for X*) and X-X (for BX) interactions. Different experiments have provided very different estimates, especially in the case of BX, depending on the methodology, temperature and size inhomogeneity of the NCs.¹⁸ In view of this, the most reliable measurements are arguably those provided by single NC emission spectroscopy at cryogenic temperatures. For CsPbBr₃ NCs with lateral sizes between 5 and 20 nm, these measurements reveal trion binding energies (Δ_{X^*}) in the range of 7 – 25 meV, and biexciton binding energies (Δ_{BX}) in the range of 25 – 40 meV.^{5–7,19–21}

Attempts to rationalize these values have been made using different theoretical models, with different descriptions of the dielectric screening and carrier-carrier interactions. In all cases, trion binding energies were in fair agreement with experiments, but biexciton ones were substantially and systematically lower.^{20,21,25} This puzzling result prompted some authors to postulate that,

in inorganic lead halide NCs, BX feel a lower effective dielectric constant than X.²⁰ The same hypothesis was adopted in later studies, for simulations to reproduce spectroscopic data.²¹

In this paper, we aim at providing more solid understanding on the origin of the unusually large Δ_{BX} values. To that end, we carry out a theoretical description of X, X* and BX in cuboidal CsPbBr₃ NCs. As in previous works, we rely on effective mass models to account for the influence of quantum confinement^{20,21,25}, and on image charges to account for dielectric confinement.²¹ Two relevant refinements are however introduced in the model. The first one refers to electronic correlations. Because CsPbBr₃ NCs are in the intermediate to weak confinement regime, carrier-carrier correlations are known to play a major role.²⁶ Here we go beyond second-order perturbation²⁵ and configuration interaction methods,^{20,21} as they have proved insufficient in other weakly confined nanostructures.²⁷ Rather, we implement a variational Quantum Monte Carlo approximation.^{28,29}

The second refinement refers to polaronic effects. Lead halide perovskites are known to have a soft lattice, such that carrier-lattice coupling becomes a significant physical factor in shaping the electronic structure. In bulk, carriers couple to optical phonons forming polarons,^{30,31} which lead to a non-hydrogenic exciton spectrum.^{32–34} Polaron signatures are also expected in NCs, but lacking dedicated theoretical simulations, their effect is not clear yet. Based on different experimental results, some authors have suggested polarons may be responsible for large and attractive Δ_{BX} ,¹⁶ large and repulsive Δ_{BX} ,¹⁷ and even break the crystal symmetry.³⁵ To shed light on this matter, here we include polaronic effects by means of a Haken-like potential, which takes into account the different dielectric screening at short and long distances from carriers.^{32,33} This approximation has proved successful in reproducing the excitonic features of bulk lead halide perovskites.³⁴ Similar polaronic potentials

have proved successful in reproducing the binding energy of X, X* and BX in layered halide perovskites and nanoplatelets.^{36–38}

Our calculations show that polaronic effects have a sizeable influence on charge-X and X-X interactions. Δ_{X^*} values in close agreement with spectroscopic data are obtained, with no need for an effective dielectric constant inside the NC. Nonetheless, Δ_{BX} remain lower than those observed in experiments. Agreement is only reached if one assumes that X and BX polarize the lattice differently, for example by imposing greater polaron radius for BX.

II. THEORETICAL MODEL

We calculate the ground state energy and wave function of excitons, negative trions and biexcitons confined in cuboidal CsPbBr₃ NCs. The Hamiltonians are based on $k \cdot p$ theory for two uncoupled (conduction and valence) bands:

$$H_X = \sum_{i=e,h} T_i + V_c(\mathbf{r}_e, \mathbf{r}_h), \quad (1)$$

$$H_{X^*} = \sum_{i=e_1, e_2, h} T_i + \sum_{i=e_1, e_2} V_c(\mathbf{r}_h, \mathbf{r}_i) + V_c(\mathbf{r}_{e_1}, \mathbf{r}_{e_2}), \quad (2)$$

$$H_{BX} = \sum_{i=e_1, e_2, h_1, h_2} T_i + \sum_{i=e_1, e_2} \sum_{j=h_1, h_2} V_c(\mathbf{r}_j, \mathbf{r}_i) + V_c(\mathbf{r}_{e_1}, \mathbf{r}_{e_2}) + V_c(\mathbf{r}_{h_1}, \mathbf{r}_{h_2}). \quad (3)$$

Here, $T_i = (\mathbf{p}_i^2 / (2m_i) + V_i)$ is the single-particle (kinetic and potential) energy operator, with m_i the effective mass and \mathbf{p}_i the momentum operator. The single-particle potential is $V_i = V_i^{conf} + V_i^{self}$, where V_i^{conf} is the spatial confining potential. In our model, we describe the NCs as a cuboid with lateral dimension L . For holes, we take $V_h^{conf} = 0$ inside the cuboid and infinite outside it. For electrons, $V_e^{conf} = E_{gap}$ (the bulk band gap) inside the cuboid and infinite outside it. V_i^{self} is the self-energy potential. $V_c(\mathbf{r}_i, \mathbf{r}_j)$ terms represent the Coulomb interaction between carriers. Both V_i^{self} and $V_c(\mathbf{r}_i, \mathbf{r}_j)$ account for dielectric confinement by using quantum box image charges, with inclusion of long-range³⁹ and short-range³⁶ interactions. They are based on a Bajaj potential⁴⁰, a Haken-like model of polaronic interactions.³³

To assist with the interpretation of the results, it is worth introducing here the basic Bajaj potential (for bulk systems, prior to inclusion of quantum and dielectric confinement). In atomic units, the potential exerted by a source charge i on a test charge j reads:⁴⁰

$$V_{ij}^{bulk}(r) = \frac{q_i q_j}{\varepsilon_s r} + \left(\frac{\varepsilon_\infty}{\varepsilon_s} \right)^\gamma \frac{q_i q_j}{\varepsilon^* r} \frac{e^{-\beta_i r} + e^{-\beta_j r}}{2}. \quad (4)$$

Here, r is the distance between charges, q the elementary charge (positive or negative) and ε_s the static dielectric

constant. The term $\left(\frac{1}{\varepsilon_\infty} - \frac{1}{\varepsilon_s} \right) = \frac{1}{\varepsilon^*}$ represents the ionic screening of carriers, with ε_∞ the high frequency dielectric constant and $\beta_i = 1/l_i$, with l_i the polaron radius of carrier i . The latter is defined as:

$$l_i = \sqrt{\frac{\hbar^2}{2m_i^b E_{LO}}}, \quad (5)$$

with E_{LO} the LO phonon energy and m_i^b the bare effective mass, which relates to the polaronic one as $m_i = m_i^b (1 + \alpha/6)$, α being the Frölich coupling constant. One should note that the first term in Eq. (4) is a Coulomb interaction with full dielectric screening (electronic plus ionic, ε_s), which prevails at long distances, $r \gg l_i$. On the other hand, the second term is a short-range (Yukawa) one, which starts prevailing at distances $r \lesssim l_i$, where the ionic contribution to dielectric screening is lost (ε_∞ dominates). The term $(\varepsilon_\infty/\varepsilon_s)^\gamma$, with γ a material dependent parameter, is the distinct trait of Bajaj potential as compared to the original Haken one. The goal of this term is to improve (phenomenologically) the estimates of exciton binding energies.⁴⁰

Hamiltonians (1)-(3) are integrated using Quantum Monte Carlo.^{41,42} Details on the evaluation of local energy and computational aspects can be found in Refs. 28, 29,38. The variational functions we integrate are defined as follows. For X, the unnormalized function reads:

$$\Psi_X = \Phi_e(\mathbf{r}_e) \Phi_h(\mathbf{r}_h) e^{-Zr_{eh}}. \quad (6)$$

Here, $\Phi_e(\mathbf{r}_e)$ and $\Phi_h(\mathbf{r}_h)$ are the non-interacting electron and hole (particle-in-box) states, which account for quantum confinement. The exponential term is a Slater correlation factor, which captures excitonic interactions. Z , the inverse of the exciton Bohr radius, is the parameter to optimize variationally. Figure 1(a) depicts the qualitative effect of increasing Z on the charge distribution of Ψ_X .

For X*, the variational function is:³⁸

$$\Psi_{X^*} = \Phi_e(\mathbf{r}_{e1}, \mathbf{r}_{e2}) \Phi_h(\mathbf{r}_h) J(r_1, r_2, r_{12}) [\alpha_{e1}\beta_{e2} - \beta_{e1}\alpha_{e2}] \sigma_h, \quad (7)$$

with $\Phi_h(\mathbf{r}_h)$ and $\Phi_e(\mathbf{r}_{e1}, \mathbf{r}_{e2})$ the analytical non-interacting-particle wave function, $\sigma_h [\alpha_{e1}\beta_{e2} - \beta_{e1}\alpha_{e2}]$ the spin function and $J(r_1, r_2, r_{12})$ the following Jastrow factor:

$$J(r_1, r_2, r_{12}) = e^{-Zs/2} \cosh(ZQt/2) e^{\frac{Zbr_{12}}{(1+Z^a r_{12})}}. \quad (8)$$

In this expression, $r_{1(2)} = |\mathbf{r}_{e1(2)} - \mathbf{r}_h|$, $r_{12} = |\mathbf{r}_{e1} - \mathbf{r}_{e2}|$, $s = r_1 + r_2$ and $t = r_1 - r_2$. The first term of J is a Slater correlation factor for electrons and holes, similar to the X case. Z is then a variational parameter, related to the electron-hole interaction strength. Its influence is depicted in Figure 1(b). The second term is to enable asymmetric electron-hole interaction for the two electrons. As can be seen in the following relation:

$$e^{-Zs/2} \cosh(ZQt/2) = (e^{-Zr_1 - Zr_2} + e^{-Zr_1 - Zr_2})/2, \quad (9)$$

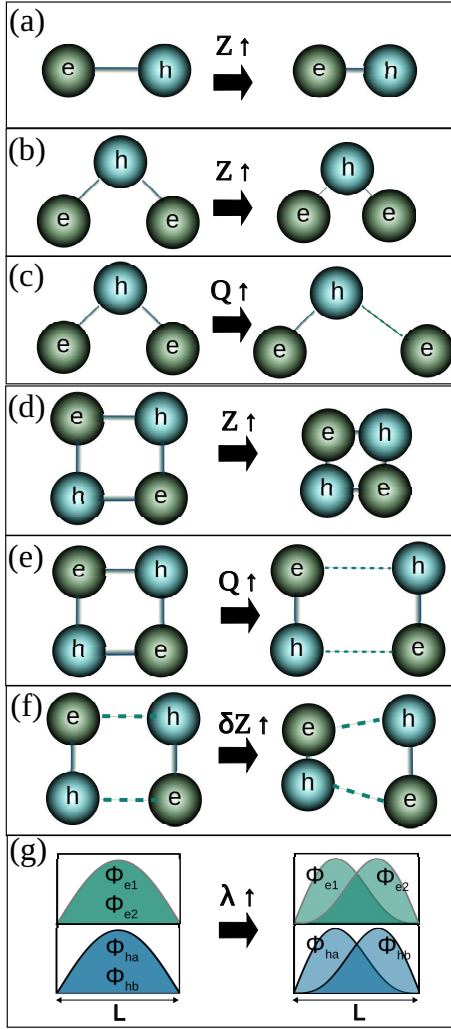


FIG. 1: Sketch of the effect of different variational parameters on (a) Ψ_X , (b-c) Ψ_{X^*} , (d-g) Ψ_{BX} . For illustration purposes, 2D charge distributions are used. Z determines the electron-hole distances. Q enables gradual dissociation of X^* and BX. For BXs, δZ introduces asymmetry between two partially dissociated Xs. λ introduces asymmetry in the envelope function of carriers with the same sign.

where $Z_1 = Z(1+Q)/2$ and $Z_2 = Z(1-Q)/2$, a non-zero Q value yields different interaction strengths. A sketch of the influence of Q in the trion charge distribution is shown in Fig. 1(c). This flexibility of the wave function has been found to play an important role for trions in layered halide perovskites, where one electron-hole pair stays within the polaronic radius, while the extra carrier orbits farther away.³⁸ Q is then our second variational parameter for X^* . The last term in J is a Padé Jastrow factor, which has the property of giving the desired limits with r_{12} . At short ranges of interaction, $r_{12} \rightarrow 0$, the term becomes $e^{b/r_{12}}$, which provides a cusp to compensate for the divergence in electron-electron Coulomb repulsion ($b > 0$). At the same time, the probability to find distant holes ($r_{12} \rightarrow \infty$) is

more likely than that of proximal holes ($r_{12} \rightarrow 0$) by a factor $(e^{b/a})^2$. We take b and a as variational parameters.

For BX, our starting variational wave function is formally the same we have successfully employed in the past to study nanoplatelets,^{29,37}

$$\Psi_{BX} = \Phi_e(\mathbf{r}_{e_1})\Phi_e(\mathbf{r}_{e_2})\Phi_h(\mathbf{r}_{h_a})\Phi_h(\mathbf{r}_{h_b}) F(r_{1a}, r_{1b}, r_{2a}, r_{2b}, r_{12}, r_{ab}). \quad (10)$$

Here, F is the correlation factor, described by:

$$F = e^{-Z\frac{(s_1+s_2)}{2}} \cosh\left(ZQ\frac{t_1-t_2}{2}\right) \times e^{Z\frac{\beta r_{12}}{1+Z\alpha r_{12}}} e^{Z\frac{\beta r_{ab}}{1+Z\alpha r_{ab}}}, \quad (11)$$

where $s_1 = r_{1a} + r_{1b}$, $s_2 = r_{2a} + r_{2b}$, $t_1 = r_{1a} - r_{1b}$ and $t_2 = r_{2a} - r_{2b}$ with $r_{12}, r_{ab}, r_{1a}, r_{1b}, r_{2a}, r_{2b}$ the interparticle distances. Z (electron-hole interaction strength), Q (degree of X-X dissociation), β and α (repulsion terms) are the variational parameters to be optimized. For the materials and geometries we consider, Z and (to a lesser extent) Q parameters are found to be major contributions on the energy. Their qualitative influence on Ψ_{BX} is sketched in Figs. 1(d) and 1(e). As shown in Fig. 1(d), increasing Z implies reducing electron-hole distances, and hence the size of the BX. As shown in Fig. 1(e), increasing Q (from $Q = 0$ to $Q = 1$), dissociates the two X forming the BX.

In some calculations, to explore if Ψ_{BX} misses electronic correlations, we introduce additional degrees of freedom. The first one takes into account that Eq. (11) is restricted to a symmetric excitonic dissociation path. That is to say, as Q grows from $Q = 0$ to $Q = 1$, the BX dissociates into two identical Xs, both with the same electron-hole attraction (Z). We can relax this restriction with an extra parameter δZ in one of the excitons, so that, while preserving the exchange of identical particles, we set $z_1 = Z$, $z_2 = Z + \delta Z$. The complete correlation factor becomes:

$$F = \frac{1}{2} \left[e^{-\frac{z_1 s_1 + z_2 s_2}{2}} \cosh\left(\frac{z_1 Q t_1 - z_2 Q t_2}{2}\right) + e^{-\frac{z_2 s_1 + z_1 s_2}{2}} \cosh\left(\frac{z_2 Q t_1 - z_1 Q t_2}{2}\right) \right] e^{-Z\frac{\beta r_{12}}{1+Z\alpha r_{12}}} e^{-Z\frac{\beta r_{ab}}{1+Z\alpha r_{ab}}}. \quad (12)$$

This function allows one to break the symmetry in the attractions while keeping unchanged the parameters for repulsion. We shall refer to δZ as the microscopic asymmetry factor. Its influence on Ψ_{BX} is sketched in Fig. 1(f).

The second degree of freedom we add will be referred to as the macroscopic asymmetry factor, λ . The goal in this case is to reduce the overlap of identical particles while keeping it unchanged for the different ones. To this

end, we do not modify the correlation factor, but rather the envelope functions, Φ_e and Φ_h . For electrons, the replacement is:

$$\begin{aligned} & \cos(kx_1) \cos(kx_2) \rightarrow \\ & [\cos(kx_1) + \lambda \sin(2kx_1)] [\cos(kx_2) - \lambda \sin(2kx_2)], \end{aligned}$$

and for holes:

$$\begin{aligned} & \cos(kx_a) \cos(kx_b) \rightarrow \\ & [\cos(kx_a) + \lambda \sin(2kx_a)] [\cos(kx_b) - \lambda \sin(2kx_b)], \end{aligned}$$

with $k = \pi/L$. We proceed in a similar way for y and z coordinates. The qualitative effect of λ is pictorially sketched on Fig. 1(g). The overlap between e_1 and h_a (e_2 and h_b) remains unity, but that between identical particles (e_1 and e_2 , h_a and h_b) becomes $(\frac{1-\lambda^2}{1+\lambda^2})^3$.

III. RESULTS

We describe CsPbBr₃ NCs using the material parameters extracted in Ref. 34. Thus, bare electron and hole masses are $m_e^b = m_h^b = 0.234 m_0$, with m_0 the free electron mass. The Frölich coupling constant is $\alpha = 2.1$, which gives polaronic masses $m_e = m_h = 0.316 m_0$. The LO phonon energy is $E_{LO} = 18$ meV. From Eq. (5), the previous parameters yield polaron radii $l_e = l_h = 3$ nm. Relative static and dynamic dielectric constants inside the NC (ϵ_{NC}) are $\epsilon_s = 16$ and $\epsilon_\infty = 4.5$. The dielectric constant of the surrounding matrix (polystyrene) is set to $\epsilon_{out} = 2.56$.²⁰ The band gap is taken from the X emission in the limit of bulk, $E_{gap} = 2.361$ eV.⁴³ In order to retrieve the bulk X binding energy, $\Delta_X^{bulk} = 33$ meV,^{43,44} the Bajaj optimization parameter is set here to $\gamma = 3/13$. Notice that this value is specific to CsPbBr₃, and hence deviates from the usual (average) value $\gamma = 3/5$ used for a number of different ionic crystals.⁴⁰

To test the validity of our model, we start by comparing the calculated X energies with the experimental band edge emission of CsPbBr₃ NCs reported in Ref. 43. Figure 2 shows the experimental data (black dots) alongside our simulations, for NCs of different sizes. A solid red line is used to represent the results of the full model, including distance-dependent dielectric screening. For comparison, we also show: (i) results neglecting dielectric confinement ($\epsilon_{out} = \epsilon_{NC}$), and (ii) results neglecting the different screening at short and long distances (i.e. replacing Eq. 4 by a simple Coulomb interaction term). The latter approximation has been used in recent theoretical studies, which took an effective dielectric constant in between the static and dynamic limit.^{20,21,25,43} The effective constant is chosen so as to fit the bulk binding energy of CsPbBr₃. With our masses, this yields $\epsilon_{eff} = 8.1$. It is inferred from Figure 2 that, on this energy scale, all levels of approximation provide reasonable agreement with experimental data. This is in contrast to nanoplatelets and

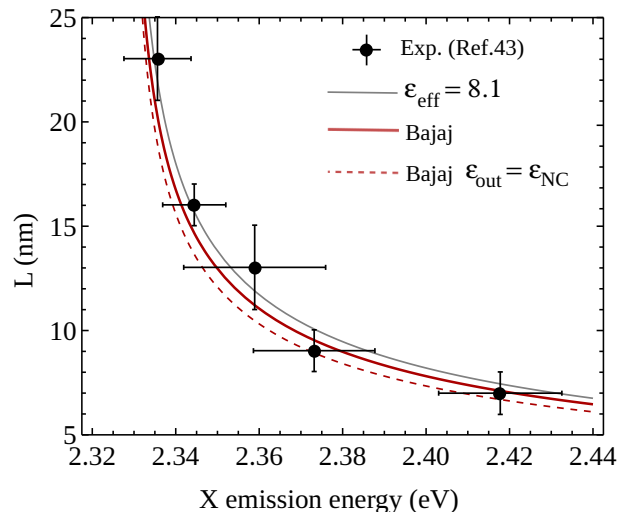


FIG. 2: Emission energy of cuboidal CsPbBr₃ NCs with different lateral sizes. Calculations under different approximations are compared with experimental values (see text). They all provide reasonable agreement

layered perovskites, where the strong quantum confinement leads to conspicuous dielectric mismatch and short-distance (Yukawa) interactions.³⁶ CsPbBr₃ NCs with the sizes we study ($L \geq 5$ nm) are in the mid- to weak confinement regime.³ The X ground state is then farther from the polystyrene region, which implies weaker dielectric confinement, and has larger size, which implies less pronounced short-distance interactions.

We next study the electronic structure and charge distribution of X* and BX, as derived from our model. The following relevant energy differences are defined:

$$\Delta_{X^*} = (E_X + E_e) - E_{X^*}, \quad (13)$$

and

$$\Delta_{BX} = 2E_X - E_{BX}, \quad (14)$$

where E_i is the ground state energy of the species i . These expressions closely correspond to the spectral shift between X* and X (BX and X) resonances in the emission spectra of NCs. They are often identified with binding energies, which is strictly true in the bulk limit.³⁸ Positive values of Δ_{X^*} and Δ_{BX} stand for bound (red-shifted) complexes. Figure 3(a) and (b) show the calculated values in NCs of different lateral side L . Red solid line represents the full calculation, discriminating short and long-distance interactions. For comparison, we also show the binding energies obtained with a Coulomb potential instead, using either ϵ_s (red dashed line) or ϵ_∞ (red dashed-dotted line) screening. In all approximations, Δ_{X^*} and Δ_{BX} increase with quantum confinement, as expected from the stronger carrier-carrier interactions in reduced space. The Bajaj potential gives intermediate values as compared to the static and dynamic screening limits. For large NCs, the energies are closer to the

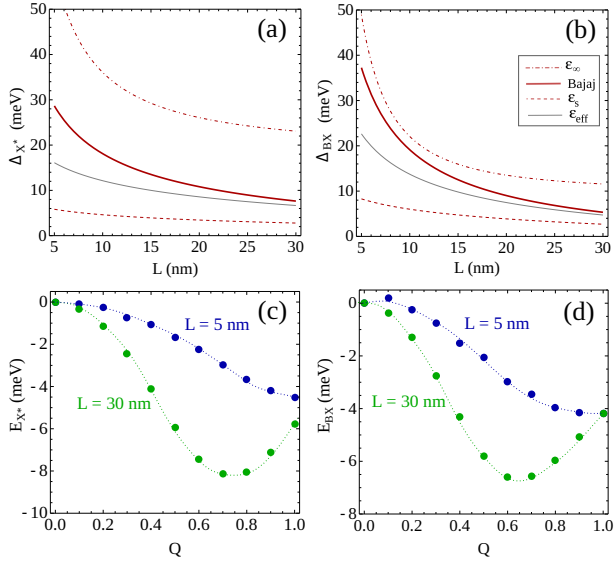


FIG. 3: (a) and (b): size dependence of X^* and BX binding energy. Red, thick lines: Bajaj potential. Dashed lines: zero polaron radius limit. Dot-dashed lines: infinite polaron radius limit. Gray lines: Coulomb potential with effective screening ($\epsilon_{eff} = 8.1$). (c) and (d): X^* and BX energy dependence on the (dimensionless) variational parameter Q , showing the extra stabilization of non-symmetric arrangements of the charge distribution. The origin of energies in each panel corresponds to that of the most symmetric structures ($Q = 0$). Lines are guides to the eye.

static limit, but they evolve towards the dynamic one as the NC becomes smaller. Likewise, using a Coulomb potential with effective screening ϵ_{eff} (gray line in the figure), as in Refs.^{20,21,25,43}, is a good approximation for large NCs, but it underestimates Δ_{X^*} and Δ_{BX} by a significant amount when confinement increases (a factor of 0.3 – 0.4 for $L = 5$ nm). It follows that the distance-dependent screening of polaronic interactions plays a significant role in determining binding energies of CsPbBr₃ NCs.

In our calculations, the ground state of X^* and BX is found to present significant charge distribution asymmetries. This can be seen in Figure 3(c) and (d), which illustrate the influence of the variational parameter Q for small ($L = 5$ nm) and large ($L = 30$ nm) NCs. For both species and all NC dimensions, the energy minima are found at non-zero values of Q . As discussed in Figure 1(c,e), this corresponds to partially dissociated excitonic complexes. Trions are then formed by an exciton plus a more distant, orbiting electron. This can be seen as a sizable ionic, as opposed to covalent, bond character. In turn, BXs are formed by two Xs , with X-X interactions being weaker than intra-X ones. This behavior is reminiscent of that found in quasi-2D lead halide perovskites.^{37,38} The absolute energy of the asymmetry corrections is smaller in NCs (< 10 meV), and yet it provides a non-negligible contribution to Δ_{X^*} and Δ_{BX} .

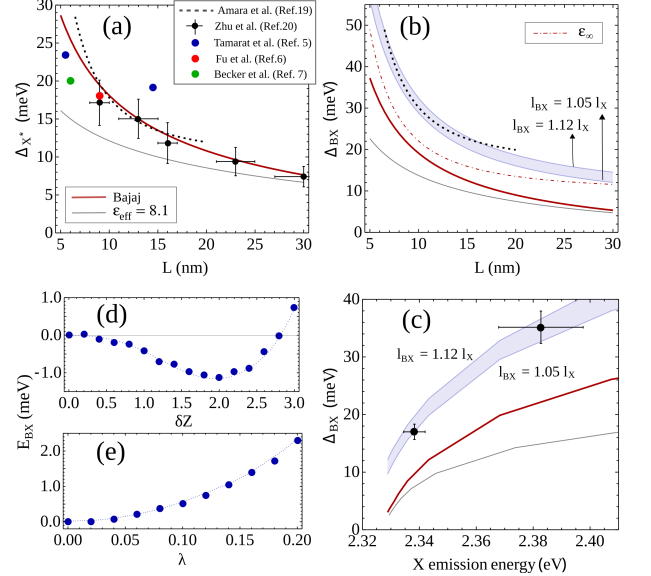


FIG. 4: (a) Size dependence of the calculated X^* binding energy (solid lines) compared to experimental data (dots, dotted line). The modified Bajaj model (red line) reproduces well the experiments. The effective screening model (gray line) underestimates the value. (b,c) Same for the BX. Experimental BX shifts from Amara et al.¹⁹ and Zhu et al.²⁰ are depicted by the dashed line and the black dots, respectively. The figure also includes the limit of dynamic screening (dot-dashed line) as well as results assuming a 5 to 12% increase of the polaron radii in the BX regime (blue shaded area). (d) and (e) BX energy dependence on the variational parameters δZ and λ , for a NC with $L = 30$ nm. The other four parameters are fixed at their optimized values for $\delta Z = \lambda = 0$.

Having analyzed the influence of polaronic (Haken-like) terms on the size-dependence of Δ_{X^*} and Δ_{BX} , we next compare the theoretical estimates with experimentally measured values. Figure 4(a) shows the comparison for X^* . The calculations using a distance-dependent screening (red solid line) are in very good agreement with data points from different experiments^{5–7,20}, as well as with the trend inferred from the systematic experiments of Amara and co-workers.¹⁹ Using an effective dielectric constant (gray line), however, underestimates the binding energies in small NCs. This is indicative that, in lead halide NCs, non-hydrogenic polaronic interactions can make a significant difference, as observed earlier in bulk^{32–34} and layered structures.^{36–38}

A completely different conclusion is drawn in the case of BXs. As shown in Figures 4(b) and 4(c), Δ_{BX} calculated with the Haken-like model (red solid line) falls short as compared to experimental values measured in Refs. 19,20. This is in spite of the binding energies being larger than those obtained with an effective dielectric constant (gray line). The discrepancy is persistent for all L values. It remains even when non-parabolic (heavier) masses⁴⁵ are used for electrons and holes (not shown), or

when larger polaron radii are assumed (see e.g. the dynamic limit, dot-dashed line in Fig. 4(b)). To verify that the origin is not related to insufficient correlation energy in our simulations, we modify our variational wave function, Eq. (10), by introducing two additional variational parameters δZ and λ . As explained in Section II, δZ introduces asymmetry through the correlation factor and λ through the envelope functions. Figure 4(d) and (e) show that neither of these factors are able to lower E_{BX} significantly. As a matter of fact, $\lambda \neq 0$ is only making the BX less stable, because the increase in kinetic energy exceeds the benefit of reduced electron-electron and hole-hole repulsions.

Having ruled out polaronic interactions and electronic correlations as the origin of the large Δ_{BX} in NCs, we can speculate on the origin of the large experimental value of Δ_{BX} . For example, in Haken-like models, originally developed for bulk, the polaron radius depends on E_{LO} —recall Eq. (5). Unlike bulk, however, NCs present low-energy phonon modes which may be related to LO phonons as well.^{19,46} If the averaged E_{LO} value turns out to be smaller for BX than for X, $l_{BX} > l_X$ may be expected. As shown in Fig. 4(b)—blue shaded area—, an increase of l_{BX} in 5-12% would suffice to match experimental Δ_{BX} values. This possibility is in line with—but different from—previous proposals, such as the effective dielectric constant felt by BX being lower than that of X.²⁰ On the other hand, the large Δ_{BX} value may be related not only to X-X interactions, but also to the shrinking of the band gap upon polaron formation, $\Delta E_{gap} = \alpha E_{LO}$,⁴⁷ provided $\alpha_{BX} > \alpha_X$. Either way, we need to assume that X and BX polarize the perovskite lattice differently. This seems to agree with the conclusions of recent time-resolved, optical-pump–electron-diffraction-probe experiments pointing out that the carrier-phonon coupling strength in lead halide perovskite lattices scales quadratically with the exciton number, so that it is stronger for BX than for X or X*.⁴⁸ Further investigations will be needed to establish the actual mechanism for the large Δ_{BX} .

IV. CONCLUSIONS

We have investigated the influence of non-hydrogenic polaronic interactions in X, X* and BX confined in CsPbBr₃ NCs, by means of a Haken-like (Bajaj) potential in an effective mass - variational Quantum Monte Carlo model. The X* ground state is formed by an exciton plus a more distant, orbiting electron. The BX ground state, in turn, is formed by two X with inter-X interaction being weaker than intra-X one. These charge distributions are reminiscent of those in layered halide perovskites.^{37,38}

It has been shown that distance-dependent dielectric screening (a signature of polaronic interactions in soft lattice materials) enhances Δ_{X^*} and Δ_{BX} in CsPbBr₃ NCs. Nonetheless, for all the NC sizes we study, Δ_{BX} is significantly smaller than that inferred from spectral shifts in single-particle experiments at cryogenic temperatures.^{5-7,19-21} That is, neither polaronic interactions, nor dielectric confinement, nor electronic correlations (all of which are well captured in our model) suffice to explain the large magnitude of Δ_{BX} . This result suggests that BXs and Xs may polarize the lattice differently, leading to different dielectric screening and/or to different renormalization of the band gap upon formation of polarons.

Acknowledgments

We are grateful to G. Rainó for discussions. We acknowledge support from Grant No. PID2021-128659NB-I00, funded by Ministerio de Ciencia e Innovación (MCIN/AEI/10.13039/501100011033 and ERDF “A way of making Europe”).

* Electronic address: climente@uji.es

¹ Q. A. Akkerman, G. Rainò, M. V. Kovalenko, and L. Manna, *Nature materials* **17**, 394 (2018).

² Q. A. Akkerman, A. L. Abdelhady, and L. Manna, *The Journal of Physical Chemistry Letters* **9**, 2326 (2018).

³ J. Butkus, P. Vashishtha, K. Chen, J. K. Gallaher, S. K. Prasad, D. Z. Metin, G. Laufersky, N. Gaston, J. E. Halpert, and J. M. Hodgkiss, *Chemistry of Materials* **29**, 3644 (2017).

⁴ S. Caicedo-Dávila, P. Caprioglio, F. Lehmann, S. Levenco, M. Stolterfoht, D. Neher, L. Kronik, and D. Abou-Ras, *Advanced Functional Materials* **33**, 2305240 (2023).

⁵ P. Tamarat, E. Prin, Y. Berezovska, A. Moskalenko, T. P. T. Nguyen, C. Xia, L. Hou, J.-B. Trebbia, M. Zacharias, L. Pedesseau, *et al.*, *Nature Communications* **14**, 229 (2023).

⁶ M. Fu, P. Tamarat, H. Huang, J. Even, A. L. Rogach, and B. Lounis, *Nano letters* **17**, 2895 (2017).

⁷ M. A. Becker, R. Vaxenburg, G. Nedelcu, P. C. Sercel, A. Shabaev, M. J. Mehl, J. G. Michopoulos, S. G. Lambrakos, N. Bernstein, J. L. Lyons, *et al.*, *Nature* **553**, 189 (2018).

⁸ Y. Wang, X. Li, J. Song, L. Xiao, H. Zeng, and H. Sun, *Advanced materials* **27**, 7101 (2015).

⁹ N. S. Makarov, S. Guo, O. Isaienko, W. Liu, I. Robel, and V. I. Klimov, *Nano letters* **16**, 2349 (2016).

¹⁰ J. A. Castañeda, G. Nagamine, E. Yassitepe, L. G. Bonato, O. Voznyy, S. Hoogland, A. F. Nogueira, E. H. Sargent, C. H. B. Cruz, and L. A. Padilha, *ACS nano* **10**, 8603 (2016).

¹¹ J. Aneesh, A. Swarnkar, V. Kumar Ravi, R. Sharma, A. Nag, and K. Adarsh, *The Journal of Physical Chem-*

- istry C **121**, 4734 (2017).
- ¹² G. Yumoto, H. Tahara, T. Kawawaki, M. Saruyama, R. Sato, T. Teranishi, and Y. Kanemitsu, *The Journal of Physical Chemistry Letters* **9**, 2222 (2018).
 - ¹³ M. N. Ashner, K. E. Shulenberger, F. Krieg, E. R. Powers, M. V. Kovalenko, M. G. Bawendi, and W. A. Tisdale, *ACS Energy Letters* **4**, 2639 (2019).
 - ¹⁴ X. Huang, L. Chen, C. Zhang, Z. Qin, B. Yu, X. Wang, and M. Xiao, *The Journal of Physical Chemistry Letters* **11**, 10173 (2020).
 - ¹⁵ X. Shen, S. Wang, C. Geng, L. Li, E. Zhao, J. Sun, W. Wu, L. An, and K. Pan, *The Journal of Physical Chemistry C* **125**, 5278 (2021).
 - ¹⁶ J. Dana, T. Binyamin, L. Etgar, and S. Ruhman, *ACS nano* **15**, 9039 (2021).
 - ¹⁷ A. K. Poonia, M. Shrivastava, W. J. Mir, J. Aneesh, A. Nag, and K. Adarsh, *Physical Review B* **104**, L161407 (2021).
 - ¹⁸ G. Lubin, G. Yaniv, M. Kazes, A. C. Ulku, I. M. Antolovic, S. Burri, C. Bruschini, E. Charbon, V. J. Yallapragada, and D. Oron, *ACS nano* **15**, 19581 (2021).
 - ¹⁹ M.-R. Amara, Z. Said, C. Huo, A. Pierret, C. Voisin, W. Gao, Q. Xiong, and C. Diederichs, *Nano Letters* **23**, 3607 (2023).
 - ²⁰ C. Zhu, T. Nguyen, S. C. Boehme, A. Moskalenko, D. N. Dirin, M. I. Bodnarchuk, C. Katan, J. Even, G. Rainò, and M. V. Kovalenko, *Advanced Materials* **35**, 2208354 (2023).
 - ²¹ K. Cho, T. Sato, T. Yamada, R. Sato, M. Saruyama, T. Teranishi, H. Suzuura, and Y. Kanemitsu, *ACS nano* **18**, 5723 (2024).
 - ²² M. Kazes, D. Nakar, I. Cherniukh, M. I. Bodnarchuk, L. G. Feld, C. Zhu, D. Amgar, G. Rainò, M. V. Kovalenko, and D. Oron, *Nano Letters* **24**, 13185 (2024).
 - ²³ J. D. Ziegler, Y. Cho, S. Terres, M. Menahem, T. Taniguchi, K. Watanabe, O. Yaffe, T. C. Berkelbach, and A. Chernikov, *Advanced Materials* **35**, 2210221 (2023).
 - ²⁴ H. Utzat, W. Sun, A. E. Kaplan, F. Krieg, M. Ginterseder, B. Spokoyny, N. D. Klein, K. E. Shulenberger, C. F. Perkinson, M. V. Kovalenko, *et al.*, *Science* **363**, 1068 (2019).
 - ²⁵ T. P. T. Nguyen, S. A. Blundell, and C. Guet, *Physical Review B* **101**, 125424 (2020).
 - ²⁶ S. Blundell and C. Guet, *Physical Review B* **105**, 155420 (2022).
 - ²⁷ J. Planelles, *Theoretical Chemistry Accounts* **136**, 81 (2017).
 - ²⁸ J. Planelles and J. I. Climente, *Computer Physics Communications* **261**, 107782 (2021).
 - ²⁹ D. F. Macias-Pinilla, J. Planelles, and J. I. Climente, *Nanoscale* **14**, 8493 (2022).
 - ³⁰ M. Puppini, S. Polishchuk, N. Colonna, A. Crepaldi, D. Dirin, O. Nazarenko, R. De Gennaro, G. Gatti, S. Roth, T. Barillot, *et al.*, *Physical Review Letters* **124**, 206402 (2020).
 - ³¹ Z. Dai, C. Lian, J. Lafuente-Bartolome, and F. Giustino, *Physical Review Letters* **132**, 036902 (2024).
 - ³² E. Menéndez-Proupin, C. L. Beltrán Ríos, and P. Wahnón, *physica status solidi (RRL)—Rapid Research Letters* **9**, 559 (2015).
 - ³³ M. Baranowski and P. Plochocka, *Advanced Energy Materials* **10**, 1903659 (2020).
 - ³⁴ M. Baranowski, A. Nowok, K. Galkowski, M. Dyksik, A. Surrente, D. Maude, M. Zacharias, G. Volonakis, S. D. Stranks, J. Even, *et al.*, *ACS Energy Letters* **9**, 2696 (2024).
 - ³⁵ D. Rossi, H. Wang, Y. Dong, T. Qiao, X. Qian, and D. H. Son, *ACS nano* **12**, 12436 (2018).
 - ³⁶ J. L. Movilla, J. Planelles, and J. I. Climente, *Nanoscale Advances* **5**, 6093 (2023).
 - ³⁷ J. I. Climente, J. L. Movilla, and J. Planelles, *The Journal of Physical Chemistry Letters* **15**, 7379 (2024).
 - ³⁸ J. I. Climente, J. L. Movilla, and J. Planelles, *The Journal of Physical Chemistry C* **128**, 17563 (2024).
 - ³⁹ T. Takagahara, *Physical Review B* **47**, 4569 (1993).
 - ⁴⁰ K. Bajaj, *Solid State Communications* **15**, 1221 (1974).
 - ⁴¹ D. Ceperley, G. V. Chester, and M. H. Kalos, *Physical Review B* **16**, 3081 (1977).
 - ⁴² R. J. Needs, M. D. Towler, N. D. Drummond, and P. L. Ríos, *Journal of Physics: Condensed Matter* **22**, 023201 (2009).
 - ⁴³ C. Zhu, S. C. Boehme, L. G. Feld, A. Moskalenko, D. N. Dirin, R. F. Mahrt, T. Stöferle, M. I. Bodnarchuk, A. L. Efros, P. C. Sercel, *et al.*, *Nature* **626**, 535 (2024).
 - ⁴⁴ Z. Yang, A. Surrente, K. Galkowski, A. Miyata, O. Portugall, R. Sutton, A. Haghighirad, H. Snaith, D. Maude, P. Plochocka, *et al.*, *ACS Energy letters* **2**, 1621 (2017).
 - ⁴⁵ P. C. Sercel, J. L. Lyons, N. Bernstein, and A. L. Efros, *The Journal of Chemical Physics* **151**, 234106 (2019).
 - ⁴⁶ C. Zhu, L. G. Feld, M. Svyrydenko, I. Cherniukh, D. N. Dirin, M. I. Bodnarchuk, V. Wood, N. Yazdani, S. C. Boehme, M. V. Kovalenko, *et al.*, *Advanced Optical Materials* **12**, 2301534 (2024).
 - ⁴⁷ C. F. Klingshirn, *Semiconductor optics* (Springer Science & Business Media, 2012).
 - ⁴⁸ N. Yazdani, M. Bodnarchuk, F. Bertolotti, N. Masciocchi, I. Furejaj, B. Guzelurk, B. Cotts, M. Zajac, G. Rainò, M. Jansen, S. Boehme, M. Yarema, M. Lin, M. Kozina, A. Reid, X. Shen, S. Weathersby, X. Wang, E. Vauthey, A. Guagliardi, M. Kovalenko, V. Wood, and A. Lindenberg, *Nature Physics* **47**, 47 (2023).